

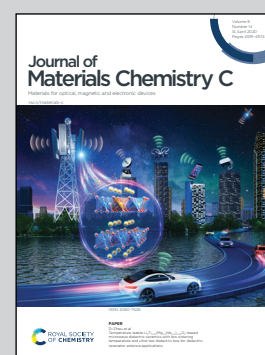


**Showcasing collaborative research from North Carolina Central University and Pennsylvania State University, USA**

Green synthesis of reduced  $\text{Ti}_3\text{C}_2\text{T}_x$  MXene nanosheets with enhanced conductivity, oxidation stability, and SERS activity

Surface engineering of  $\text{Ti}_3\text{C}_2\text{T}_x$  MXenes enhances electrical conductivity, oxidation stability and surface-enhanced Raman scattering activity. The reduced MXene nanosheets are uniquely suitable for applications that employ high electronic conductivity, such as electrode materials for batteries and supercapacitors, photodetectors, and SERS-based sensors.

**As featured in:**



See Fei Yan *et al.*,  
*J. Mater. Chem. C*, 2020, 8, 4722.

Cite this: *J. Mater. Chem. C*, 2020, **8**, 4722

## Green synthesis of reduced $\text{Ti}_3\text{C}_2\text{T}_x$ MXene nanosheets with enhanced conductivity, oxidation stability, and SERS activity†

Tej B. Limbu,<sup>a</sup> Basant Chitara,<sup>a</sup> Jason D. Orlando,<sup>a</sup> Martha Y. Garcia Cervantes,<sup>a</sup> Shalini Kumari,<sup>b</sup> Qi Li,<sup>b</sup> Yongan Tang<sup>c</sup> and Fei Yan<sup>\*a</sup>

Transition metal carbides (MXenes) are an emerging family of highly conductive two-dimensional materials with additional functional properties introduced by surface terminations. Further modification of the surface terminations makes MXenes even more appealing for practical applications. Herein, we report a facile and environmentally benign synthesis of reduced  $\text{Ti}_3\text{C}_2\text{T}_x$  MXene ( $r\text{-Ti}_3\text{C}_2\text{T}_x$ ) via a simple treatment with L-ascorbic acid at room temperature.  $r\text{-Ti}_3\text{C}_2\text{T}_x$  shows a six-fold increase in electrical conductivity, from  $471 \pm 49$  for regular  $\text{Ti}_3\text{C}_2\text{T}_x$  to  $2819 \pm 306 \text{ S m}^{-1}$  for the reduced version. Additionally, we show an enhanced oxidation stability of  $r\text{-Ti}_3\text{C}_2\text{T}_x$  as compared to regular  $\text{Ti}_3\text{C}_2\text{T}_x$ . An examination of the surface-enhanced Raman scattering (SERS) activity reveals that the SERS enhancement factor of  $r\text{-Ti}_3\text{C}_2\text{T}_x$  is an order of magnitude higher than that of regular  $\text{Ti}_3\text{C}_2\text{T}_x$ . The improved SERS activity of  $r\text{-Ti}_3\text{C}_2\text{T}_x$  is attributed to the charge transfer interaction between the MXene surface and probe molecules, re-enforced by an increased electronic density of states (DOS) at the Fermi level of  $r\text{-Ti}_3\text{C}_2\text{T}_x$ . The findings of this study suggest that reduced MXene could be a superior choice over regular MXene, especially for the applications that employ high electronic conductivity, such as electrode materials for batteries and supercapacitors, photodetectors, and SERS-based sensors.

Received 22nd December 2019,  
Accepted 3rd March 2020

DOI: 10.1039/c9tc06984d

rsc.li/materials-c

### 1. Introduction

Since their discovery in 2011,<sup>1</sup> titanium carbides, also called MXenes, a two-dimensional (2D) layered material, have attracted increasing attention from the scientific community, due to their exciting properties such as high metallic-like conductivity, good environmental and chemical stability, and controllable surface hydrophilicity.<sup>2,3</sup> Subsequently, several other species of the MXene family<sup>4–8</sup> have been discovered and synthesized in laboratories by top-down approaches starting with a three-dimensional parent

material known as MAX. MAX phases are transition metal carbides, nitrides, or carbonitrides with the general formula  $\text{M}_{n+1}\text{AX}_n$ , where  $n = 1, 2, \text{ or } 3$ , M is a transition metal, A is an A group element (mainly 13 and 14 group), and X is C and/or N. After removal of the A layers in MAX phases by chemical etching, the obtained 2D materials are regarded as MXenes, which are usually represented by the general formula  $\text{M}_{n+1}\text{X}_n\text{T}_x$ , where  $\text{T}_x$  is the surface termination acquired during the chemical etching process. Depending upon the type of M and X elements, and surface terminations, various members of the MXene family are known to exhibit quite different physical properties and chemical behavior; from metallic to semiconducting, or topological insulators, and even magnetic.<sup>6,7,9</sup> Due to their diverse and exciting properties, MXenes have been explored for a myriad of applications, including energy storage devices,<sup>10–12</sup> catalysis,<sup>5,13,14</sup> water desalination,<sup>15</sup> transparent conductors,<sup>16,17</sup> light absorbers,<sup>3</sup> electromagnetic interference shielding,<sup>18</sup> photodetection,<sup>19</sup> and surface-enhanced Raman scattering (SERS) detection,<sup>4,20,21</sup> among others.

Among a wide variety of MXene species,  $\text{Ti}_3\text{C}_2\text{T}_x$  MXene is reported to have shown the highest electrical conductivity<sup>22</sup> and has been studied most extensively. It possesses impressive metallic-like conductivity comparable to those of reduced graphene oxide (GO) and carbon nanotubes,<sup>23,24</sup> and for most applications,

<sup>a</sup> Department of Chemistry and Biochemistry, North Carolina Central University, Durham, NC 27707, USA. E-mail: fyan@ncsu.edu, tejblimbu@gmail.com

<sup>b</sup> Department of Physics, The Pennsylvania State University, University Park, PA 16802, USA

<sup>c</sup> Department of Mathematics and Physics, North Carolina Central University, Durham, NC 27707, USA

† Electronic supplementary information (ESI) available: Deconvolution of XPS fine peaks for Ti2p, O1s, and C1s; details of electrical measurements; calculation of electrical conductivity and contact resistivity; thickness measurement for  $\text{Ti}_3\text{C}_2\text{T}_x$  and  $r\text{-Ti}_3\text{C}_2\text{T}_x$  films; MXene oxidation stability test; SEM analysis of degraded  $\text{Ti}_3\text{C}_2\text{T}_x$  and  $r\text{-Ti}_3\text{C}_2\text{T}_x$ ; Raman spectra of disordered carbon material formed on MXene; photographs of the SERS substrates on PVDF filter membranes; UV-vis absorption spectra of CV, MB, and R6B; examination of plasmonic absorption in  $\text{Ti}_3\text{C}_2\text{T}_x$  and  $r\text{-Ti}_3\text{C}_2\text{T}_x$ . See DOI: 10.1039/c9tc06984d



such as electrode materials for batteries, supercapacitors, transparent conductors, plasmonic devices, photodetectors, and SERS substrates, high electrical conductivity is desired. Interestingly, the conductivity of MXenes can be further increased by de-intercalation and surface de-functionalization.<sup>6</sup> Hart *et al.*<sup>6</sup> demonstrated by *in situ* vacuum annealing, electrical biasing, spectroscopic analysis, and transmission electron microscopy (TEM) that the loss of –OH and –F terminations in  $\text{Ti}_3\text{C}_2\text{T}_x$  MXene improves electronic conductivity. This result is consistent with a literature report<sup>25</sup> that by density functional theory simulation showed that surface functionalization with –OH, –H, –F, and –O on  $\text{Ti}_3\text{C}_2$  MXene reduces the density of states (DOS) at the Fermi level, thereby reducing the conductivity. This implies that there exists plenty of room for further enhancement of the electrical conductivity of MXene by surface modification. Reduction of MXenes could be a new approach to tailor the properties and conductivity enhancement, in analogy with the reduction of insulating GO to highly conducting reduced-graphene oxide (r-GO).<sup>26,27</sup> Yoon *et al.*<sup>2</sup> showed that Li-ethylenediamine (Li-EDA) treatment on  $\text{Ti}_3\text{C}_2\text{T}_x$  removes most of the F and OH terminations and  $\text{Ti}^{4+}$  chemical states are changed to  $\text{Ti}^{3+}$ , and the reduction of  $\text{Ti}_3\text{C}_2\text{T}_x$  MXene produces a Pauli paramagnetic character. Although this work showed an effective method of  $\text{Ti}_3\text{C}_2\text{T}_x$  MXene reduction, the use of Li-EDA as a reducing agent required a glove-box environment for safety purposes. This indicates a need for a safer, reproducible, and easily accessible method for the MXene reduction process.

Among several potential applications, MXenes have shown promise for making cheap and efficient SERS substrates.<sup>4,20,21,28</sup> SERS is a non-destructive and highly sensitive technique for molecular detection at trace amounts. Although noble metal nanostructure-based SERS substrates have shown an ultrahigh enhancement factor (EF) of  $10^{14}$ ,<sup>29</sup> the high cost of production limits their wide use for practical purposes. MXenes, which are produced by simple solution processing methods with relatively cheap precursors, can be an alternative material for commercial SERS substrates. Sarycheva *et al.*<sup>20</sup> showed that  $\text{Ti}_3\text{C}_2\text{T}_x$  MXene-based SERS substrates enhanced the Raman signal of common organic dyes by as much as  $10^6$ . Soundiraraju *et al.*<sup>4</sup> reported even more interesting SERS results with titanium nitride ( $\text{Ti}_2\text{NT}_x$ ) MXene. They found an EF of  $10^{12}$  using rhodamine 6G as a probe compound on a SERS substrate made by coating paper with  $\text{Ti}_2\text{NT}_x$ . Such a high EF is good enough for single molecule detection, indicating a potential use of MXenes for replacing expensive SERS substrates made from noble metal nanostructures.

Despite their exciting physical and electrochemical properties, it is widely known that MXenes have a weak chemical and environmental stability,<sup>30–35</sup> which can limit their use for practical applications. Because of the spontaneous and rapid oxidation issue in water and air, better ways of storing MXenes have also been explored and suggested.<sup>30,32,35</sup> However, it would be even more interesting if the cause of oxidation could be identified and the MXene crystals could be engineered to make them shelf-stable, or if one could discover a state-of-the-art route to synthesize chemically and environmentally stable MXenes.

In this work, we demonstrate a green protocol for the room temperature synthesis of reduced  $\text{Ti}_3\text{C}_2\text{T}_x$  MXene (r- $\text{Ti}_3\text{C}_2\text{T}_x$ ) *via* a simple L-ascorbic acid treatment, which is facile and highly reproducible. We show a significant modification of the properties of r- $\text{Ti}_3\text{C}_2\text{T}_x$  with enhanced electrical conductivity and oxidation stability as compared to that of the  $\text{Ti}_3\text{C}_2\text{T}_x$  MXene ( $\text{Ti}_3\text{C}_2\text{T}_x$ ) prepared by conventional methods,<sup>1,20,36</sup> showing reduced MXene as a primary choice for use in several applications that employ high electronic conductivity. We also report an application of r- $\text{Ti}_3\text{C}_2\text{T}_x$  as a SERS substrate and demonstrate an improvement in the SERS EF by an order of magnitude compared to that of  $\text{Ti}_3\text{C}_2\text{T}_x$ .

## 2. Experimental section

### 2.1 Synthesis of $\text{Ti}_3\text{C}_2\text{T}_x$

To synthesize r- $\text{Ti}_3\text{C}_2\text{T}_x$ , we started with etching of Al layers in  $\text{Ti}_3\text{AlC}_2$  MAX powder purchased from Carbon-Ukraine (Y-Carbon, Ltd). The reduction process is preceded by etching and MXene delamination. The etching of Al layers and delamination of MXene were carried out following the methods described in a published report<sup>36</sup> with a slight modification. Briefly, 0.5 g of  $\text{Ti}_3\text{AlC}_2$  MAX powder was slowly added to 10 ml of 30% hydrofluoric acid (HF) (ACROS Organics, 48–51% solution in water) under a gentle and constant stirring condition with the help of a Teflon magnetic bar, and the stirring was continued for 7 hours. The solution was then washed one time with deionized (DI) water by centrifugation at a speed of 3500 rpm for 30 minutes and the water-like supernatant was removed. The sediment was then further washed with at least 5 liters of DI water *via* vacuum-assisted filtration using a polyvinylidene difluoride (PVDF) filter membrane with 0.22  $\mu\text{m}$  pore size (Durapore, Millipore) until the pH of the filtrate was lowered to  $\sim 6.5$ . The cleaned sediment was then dried in the same filter cup by placing it in a vacuum desiccator for 24 hours. For the delamination process, 100 mg of  $\text{Ti}_3\text{C}_2\text{T}_x$  powder was put into 20 ml of 1% tetramethylammonium hydroxide (TMAOH) (Alfa Aesar, Electronic Grade, 99.9999% (metal basis) liquid) solution and was shaken for 24 hours. After 24 hours of shaking, the solution was centrifuged at 5000 rpm for 30 minutes to separate out the unwanted brown solution containing TMAOH. The centrifugation process was repeated several times until the pH of the supernatant solution was decreased to  $\sim 7$ . The MXene solution was then centrifuged at 3500 rpm for 5 minutes to separate out the bigger and unetched particles, and the stable MXene colloidal solution was collected for further processing.

### 2.2 Green synthesis of r- $\text{Ti}_3\text{C}_2\text{T}_x$

For the reduction process, first, DI water was added to the obtained MXene colloidal solution to make a total volume of 40 ml. The solution was shaken and divided into two equal volumes, 20 ml each for  $\text{Ti}_3\text{C}_2\text{T}_x$  and r- $\text{Ti}_3\text{C}_2\text{T}_x$ . One part was further centrifuged to extract a slurry and freeze-dried to obtain a powder material for characterization. The obtained  $\text{Ti}_3\text{C}_2\text{T}_x$  powder was weighed to be  $\sim 25$  mg. The other part, which was expected to contain the same amount of  $\text{Ti}_3\text{C}_2\text{T}_x$  ( $\sim 25$  mg) in 20 ml of water was mixed with 1 g of L-ascorbic acid

(Fisher Scientific, Reagent Grade) and shaken for 5 hours. After 5 hours of treatment with L-ascorbic acid, the solution was centrifuged several times at 5000 rpm for 30 minutes to remove the acidic solution. Finally, a slurry of r-Ti<sub>3</sub>C<sub>2</sub>T<sub>x</sub> nanosheets was extracted and freeze-dried to obtain the r-Ti<sub>3</sub>C<sub>2</sub>T<sub>x</sub> powder for characterization. In order to obtain Ti<sub>3</sub>C<sub>2</sub>T<sub>x</sub> and r-Ti<sub>3</sub>C<sub>2</sub>T<sub>x</sub> colloidal solutions for film preparation on SiO<sub>2</sub>/Si and paper, the synthesis process was repeated, and instead of freeze-drying, the slurries of MXene nanosheets were dissolved in a suitable amount of methanol.

### 2.3 Fabrication of Ti<sub>3</sub>C<sub>2</sub>T<sub>x</sub>/r-Ti<sub>3</sub>C<sub>2</sub>T<sub>x</sub> films

To fabricate the films of Ti<sub>3</sub>C<sub>2</sub>T<sub>x</sub> and r-Ti<sub>3</sub>C<sub>2</sub>T<sub>x</sub> on SiO<sub>2</sub>/Si substrates, the slurries of Ti<sub>3</sub>C<sub>2</sub>T<sub>x</sub> and r-Ti<sub>3</sub>C<sub>2</sub>T<sub>x</sub> nanosheets were dissolved in a suitable amount of methanol separately in two different glass vials to obtain dense colloidal solutions. The dense colloidal solutions of Ti<sub>3</sub>C<sub>2</sub>T<sub>x</sub> and r-Ti<sub>3</sub>C<sub>2</sub>T<sub>x</sub> nanosheets were drop casted on oxygen plasma-cleaned SiO<sub>2</sub>/Si substrates followed by subsequent heating at 60 °C by placing the samples on a hot plate. Ti<sub>3</sub>C<sub>2</sub>T<sub>x</sub> and r-Ti<sub>3</sub>C<sub>2</sub>T<sub>x</sub> films on paper substrates were fabricated on PVDF filter paper with a pore size of 0.22 μm (Durapore, Millipore) employing vacuum-assisted filtration.

### 2.4 Characterization of Ti<sub>3</sub>C<sub>2</sub>T<sub>x</sub>/r-Ti<sub>3</sub>C<sub>2</sub>T<sub>x</sub>

Characterization of Ti<sub>3</sub>C<sub>2</sub>T<sub>x</sub>/r-Ti<sub>3</sub>C<sub>2</sub>T<sub>x</sub> samples was performed by using Raman spectroscopy (Horiba LabRAM Evolution RAMAN microscope), atomic force microscopy (AFM) (Horiba Smart SPM Atomic Force Microscope), UV-visible spectroscopy

(VWR, UV-3100PC Spectrophotometer), scanning electron microscopy (SEM) (FEI Verios 460L), TEM (FEI Talos F200X, 200 KV accelerating voltage), X-ray diffractometry (XRD) (Rigaku Smart-Lab X-ray Diffractometer), and X-ray photoelectron spectroscopy (XPS) (SPECS FlexMod XPS, Mg Kα excitation (1254 eV)). Ti(20 nm)/Au(300 nm) contact pads were deposited on the fabricated MXene films by using electron beam evaporation. Electrical properties were studied by employing transmission line measurements with two probes in a probe station (EVERBEING) equipped with a Keithley analyzer (4200A-SCS). For the test of oxidation stability, the dried and stored Ti<sub>3</sub>C<sub>2</sub>T<sub>x</sub> and r-Ti<sub>3</sub>C<sub>2</sub>T<sub>x</sub> powders were re-dispersed in water at a concentration of 15 mg/10 ml, sonicated for 10 minutes and left open in an ambient atmosphere for several days. The stability test was repeated with another concentration, 5 mg/10 ml of water for confirmation. The SERS measurements were performed using a Raman spectrometer (Horiba LabRAM Evolution RAMAN microscope) with 532 nm laser excitation and a 100× objective lens with an integration time of 20 s. Raman enhancement of Ti<sub>3</sub>C<sub>2</sub>T<sub>x</sub> and r-Ti<sub>3</sub>C<sub>2</sub>T<sub>x</sub> was examined with three dye molecules, *i.e.*, crystal violet (CV) (ACROS Organics), methylene blue (MB) (ACROS Organics), and rhodamine 6G (R6G) (ACROS Organics).

## 3. Results and discussion

### 3.1 Synthesis and characterization

Fig. 1 schematically summarizes the synthesis route of r-Ti<sub>3</sub>C<sub>2</sub>T<sub>x</sub>. Etching of Al layers in the Ti<sub>3</sub>AlC<sub>2</sub> MAX phase (Fig. 1a) with HF

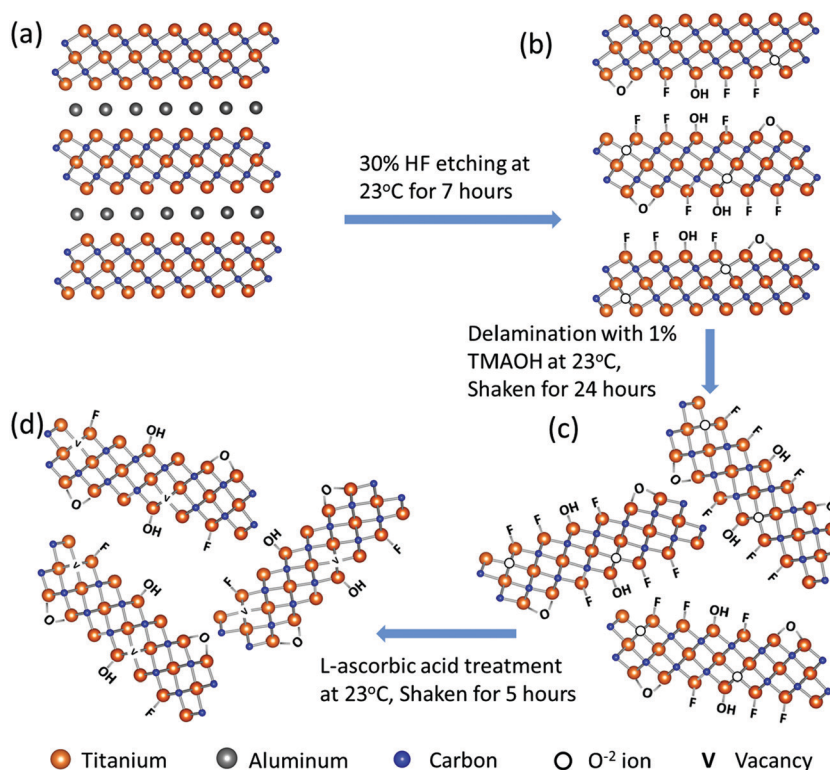


Fig. 1 Schematic diagram of r-Ti<sub>3</sub>C<sub>2</sub>T<sub>x</sub> synthesis.

produces 2D crystals of titanium carbide with  $-O$ ,  $-OH$ , and  $-F$  terminations (Fig. 1b). The  $Ti_3C_2T_x$  layers are still bound to each other by a weak hydrogen or van der Waals force between  $T_x$  (OH, F, O) terminations of two adjacent MXene layers.<sup>1,36</sup> Upon intercalation with tetramethylammonium ions during delamination using TMAOH, the  $Ti_3C_2T_x$  layers are separated into free standing particles (Fig. 1c). Treatment of colloidal  $Ti_3C_2T_x$  solution with L-ascorbic acid changes the surface chemistry of MXene nanosheets to give rise to reduced  $Ti_3C_2T_x$  (Fig. 1d). We note that we have followed the model presented by Yoon *et al.*<sup>2</sup> to describe the surface chemistry changes in the 2D  $Ti_3C_2T_x$  due to HF etching and reduction processes as depicted in Fig. 1b–d, which will be discussed later in detail.

SEM images in Fig. 2a and b show that 3D  $Ti_3AlC_2$  MAX particles are changed to accordion-like multilayer  $Ti_3C_2T_x$  structures indicating that Al layers in the  $Ti_3AlC_2$  MAX phase are etched out by HF. Fig. 2c and d show fabric-like SEM micrographs of  $Ti_3C_2T_x$  powder before and after L-ascorbic acid treatment, respectively. The tapping mode AFM image (Fig. 2e) of  $Ti_3C_2T_x$  nanosheets deposited onto  $SiO_2/Si$  substrates shows that the majority of the sheets are large with a lateral dimension of about 1  $\mu m$  and 2 to 6 nm height corresponding to 1 to 3 layers. Fig. 1f shows a high magnification TEM image of a 2D  $Ti_3C_2T_x$  nanosheet suspended over a holey carbon grid, and its inset shows the selected area electron diffraction pattern with a

six-fold reflection spot corresponding to the hexagonal crystal symmetry of  $Ti_3C_2T_x$ .

XPS analysis of the samples shows a clear difference among the  $Ti_3AlC_2$  MAX phase,  $Ti_3C_2T_x$ , and  $r-Ti_3C_2T_x$ . The XPS survey spectrum (Fig. 3a) of the  $Ti_3AlC_2$  MAX phase (black) shows a peak at 77.0 eV corresponding to Al, which, however, is below the detection limit in the spectra of  $Ti_3C_2T_x$  (red), and  $r-Ti_3C_2T_x$  (blue). This indicates that HF treatment on  $Ti_3AlC_2$  MAX powder removes most of the Al layers. The survey spectra of  $Ti_3C_2T_x$  show a F peak at 685.0 eV with 8.1 atomic%, due to the addition of fluorine during HF etching.<sup>36</sup> After treatment with L-ascorbic acid, the fluorine amount significantly decreases to 3.8%. This shows that L-ascorbic acid treatment significantly changes the surface chemistry of  $Ti_3C_2T_x$ , similar to the results in a published report,<sup>2</sup> where Li-EDA treatment is shown to remove a significant amount of F termination from  $Ti_3C_2T_x$ . Fig. 3b depicts a high-resolution peak of Ti2p ranging from 454.8 to 464.8 eV for  $Ti_3AlC_2$  MAX phase (black),  $Ti_3C_2T_x$  (red), and  $r-Ti_3C_2T_x$  (blue). Deconvolution (Fig. S1a and b, ESI<sup>†</sup>) shows that Ti2p<sub>3/2</sub> peaks appear between 454.8 and 459.0 eV and the peaks beyond 459.0 eV are their corresponding doublets (Ti2p<sub>1/2</sub>). These peaks have been assigned to Ti, Ti<sup>2+</sup>, Ti<sup>3+</sup>, and Ti<sup>4+</sup> chemical states as in the literature.<sup>2,37,38</sup> The peaks appearing at 454.8 eV (460.3 eV) and 459.0 eV (464.9 eV) for  $Ti_3C_2T_x$  are assigned to Ti bonded to C of  $Ti_3C_2$  crystal and  $TiO_2$  resulting from surface oxidation, respectively.<sup>37,38</sup> For  $Ti_3C_2T_x$ , the component peak at 459.0 eV (464.9 eV) is also largely contributed by Ti<sup>4+</sup> chemical states of Ti atoms surrounded by the O<sup>2-</sup> ions in the lattice, which occurs due to the replacement of some carbons by oxygen in the crystal during the etching process.<sup>2</sup> This fact is supported by the increased intensity ratio of Ti<sup>4+</sup> to Ti–C peaks for  $Ti_3C_2T_x$  compared to the  $Ti_3AlC_2$  MAX phase. The peaks at 456.4 eV (461.5 eV) and 458.2 eV (263.5 eV) are assigned to Ti<sup>2+</sup> and Ti<sup>3+</sup> chemical states, respectively.<sup>2,38,39</sup> One of the main purposes of XPS analysis is to assess the difference between  $Ti_3C_2T_x$  and  $r-Ti_3C_2T_x$ . Interestingly, we observed clear changes in the intensities of Ti<sup>3+</sup> and Ti<sup>4+</sup> components. In contrast to  $Ti_3C_2T_x$  (red),  $r-Ti_3C_2T_x$  (blue) shows a high intensity of Ti<sup>3+</sup> peak at 458.2 eV (463.7 eV) with a diminished Ti<sup>4+</sup> peak at 459.0 eV (464.7 eV), indicating a reduction of Ti<sup>4+</sup> chemical states to Ti<sup>3+</sup> under L-ascorbic acid treatment.

The O1s fine spectra (Fig. S1c and d, ESI<sup>†</sup>) of both  $Ti_3C_2T_x$  and  $r-Ti_3C_2T_x$  have been fitted with four different components peaking at 530.4, 531.6, 532.6, and 533.7 eV and are assigned to  $TiO_2$ , Ti–O, Ti–OH, and adsorbed H<sub>2</sub>O molecules, respectively. The deconvolution clearly shows that the  $TiO_2$  component decreases upon reduction of  $Ti_3C_2T_x$  with L-ascorbic acid, and the center of gravity of the O1s fine spectrum of  $r-Ti_3C_2T_x$  is slightly shifted to a higher energy with respect to  $Ti_3C_2T_x$ , consistent with a published report.<sup>2</sup> Some changes can also be seen between C1s XPS spectra of  $Ti_3C_2T_x$  and  $r-Ti_3C_2T_x$  (see Fig. S1e and f, ESI<sup>†</sup>). The C1s fine spectrum of  $Ti_3C_2T_x$  has been deconvoluted into five components peaking at 282.4, 284.5, 285.6, 286.8, and 288.9 eV and they are assigned to Ti–C bonds in  $Ti_3C_2T_x$  crystal, C–C, CH<sub>x</sub>, C–O, and COOH, respectively. The spectrum of  $r-Ti_3C_2T_x$  has been deconvoluted with the same components,

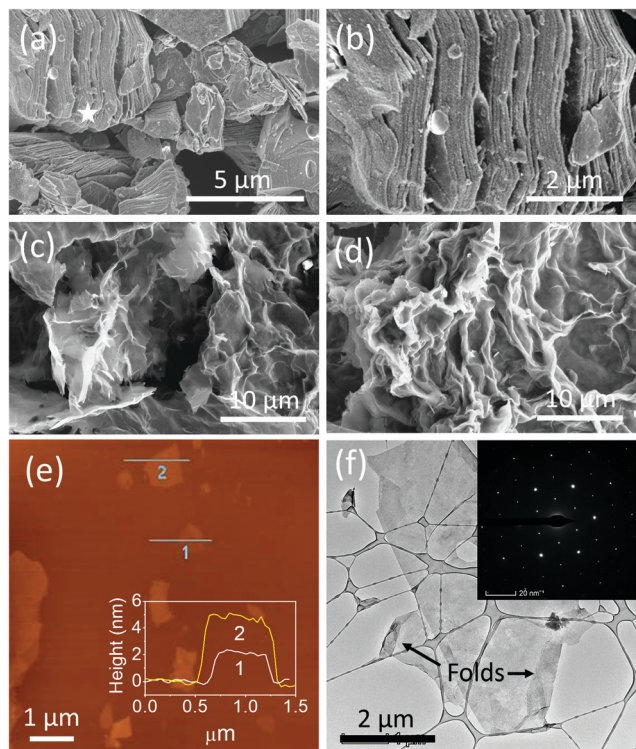


Fig. 2 (a and b) SEM micrographs of  $Ti_3C_2T_x$  after HF-etching of  $Ti_3AlC_2$  MAX phase, (c and d) SEM micrographs of  $Ti_3C_2T_x$  and  $r-Ti_3C_2T_x$  powders, respectively, (e) Tapping mode AFM image of  $Ti_3C_2T_x$  nanosheets on  $SiO_2/Si$ , and (f) high magnification TEM image of a  $Ti_3C_2T_x$  nanosheet suspended over a holey carbon grid. The inset shows the selected area electron diffraction (SAED) pattern.



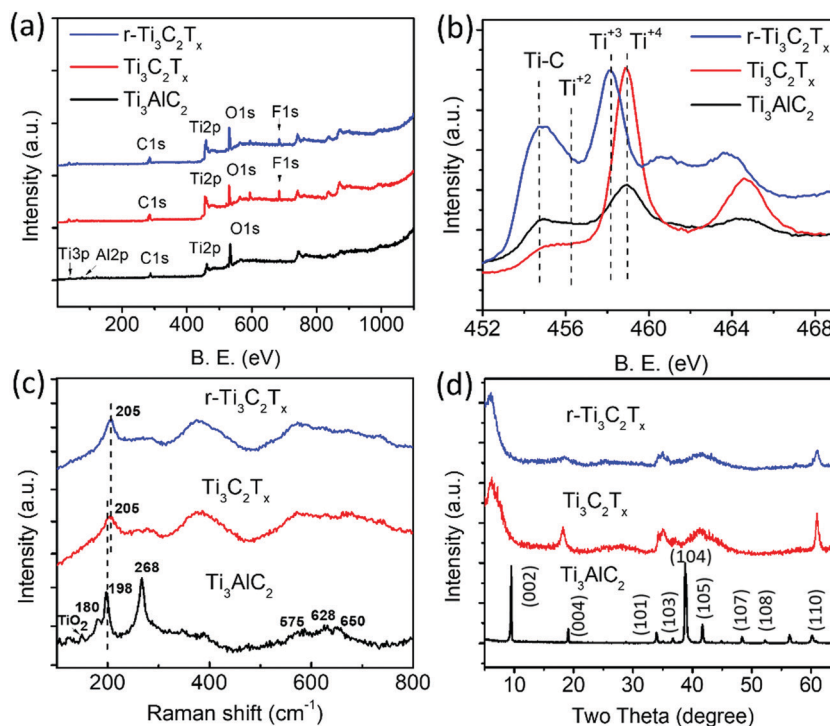


Fig. 3 (a) XPS survey spectra, (b) high resolution XPS spectra of Ti2p region, (c) Raman spectra, and (d) XRD patterns, respectively, of  $\text{Ti}_3\text{AlC}_2$  MAX phase (black),  $\text{Ti}_3\text{C}_2\text{T}_x$  (red), and  $r\text{-Ti}_3\text{C}_2\text{T}_x$  (blue).

but the peak intensity ratio of C bonds in the components C-C,  $\text{CH}_x$ , C-O, and COOH altogether to that of Ti-C alone increases compared to  $\text{Ti}_3\text{C}_2\text{T}_x$ , similar to the results in a published report.<sup>2</sup>

Fig. 3c shows the normalized Raman spectra of  $\text{Ti}_3\text{AlC}_2$  MAX phase (black),  $\text{Ti}_3\text{C}_2\text{T}_x$  (red), and  $r\text{-Ti}_3\text{C}_2\text{T}_x$  (blue).  $\text{Ti}_3\text{AlC}_2$  MAX phase shows six distinct Raman bands, among which three intense bands occurring at 180, 198, and  $268\text{ cm}^{-1}$  are associated with the vibrations of Ti and Al bonds and three shallow bands occurring at 575, 628, and  $650\text{ cm}^{-1}$  are associated with Ti-C bonds.<sup>1,40</sup> A small peak at  $149\text{ cm}^{-1}$  is the  $E_g$  vibrational mode of anatase phase  $\text{TiO}_2$  particles<sup>41</sup> formed due to spontaneous oxidation of surface titanium atoms. Note that this peak is very intense relative to the MXene band intensity when there is a sufficient amount of  $\text{TiO}_2$ ,<sup>41</sup> and hence even with a small amount present, it is easily detectable.  $\text{Ti}_3\text{C}_2\text{T}_x$  and  $r\text{-Ti}_3\text{C}_2\text{T}_x$  show a broadened peak at  $205\text{ cm}^{-1}$ , which is assigned to the Ti-Al vibrational mode occurring at  $198\text{ cm}^{-1}$  in MAX phase and is slightly blue-shifted, due to a phonon stiffening effect as the crystals are thinned down to the nanoscale. Apparently, our observation suggests that this Raman peak is visible even at a small amount of Al in MXene crystals, which is below the detection limit of XPS. The three peaks occurring at 575, 628, and  $650\text{ cm}^{-1}$  in MAX phase are merged and red-shifted in  $\text{Ti}_3\text{C}_2\text{T}_x$  and  $r\text{-Ti}_3\text{C}_2\text{T}_x$ , as observed previously.<sup>1,40</sup>

The XRD patterns (Fig. 3d) show that several peaks are not observed for  $\text{Ti}_3\text{C}_2\text{T}_x$  (red), including the most intense one appearing at  $39.0^\circ$  due to the disappearance of the non-basal crystal planes upon removal of Al layers by HF etching. Consistent with the reports,<sup>1,28</sup> we observed a broadening, loss of intensity,

and shift of the peaks to lower angles for (00l) peaks such as (002) and (004). The peaks appearing in the range of  $33\text{--}45^\circ$  broaden so significantly that they look merged together. The most prominent change is a huge shift of the (002) peak from  $9.5^\circ$  in  $\text{Ti}_3\text{AlC}_2$  MAX to  $6.5^\circ$  in  $\text{Ti}_3\text{C}_2\text{T}_x$ , owing to the removal of Al layers and the introduction of surface terminations (-F, -O, -OH).<sup>36</sup>  $r\text{-Ti}_3\text{C}_2\text{T}_x$  shows similar XRD peaks to  $\text{Ti}_3\text{C}_2\text{T}_x$ , except that the (002) peak is further shifted to a slightly lower angle,  $6.0^\circ$  in  $r\text{-Ti}_3\text{C}_2\text{T}_x$ , which could be attributed to a further increase of the c-lattice spacing upon removal of F terminations.

### 3.2 Enhanced electrical conductivity of $r\text{-Ti}_3\text{C}_2\text{T}_x$

Fig. 4a shows a SEM micrograph of  $r\text{-Ti}_3\text{C}_2\text{T}_x$  with Ti/Au contact pads. More detailed images of  $\text{Ti}_3\text{C}_2\text{T}_x$  and  $r\text{-Ti}_3\text{C}_2\text{T}_x$  are presented in Fig. S2, ESI† High magnification SEM images of the  $\text{Ti}_3\text{C}_2\text{T}_x$  and  $r\text{-Ti}_3\text{C}_2\text{T}_x$  films are presented in the insets of Fig. 4b and c, respectively. Fig. 4b and c present the plots of the measured total resistance vs. contact pad spacing for  $\text{Ti}_3\text{C}_2\text{T}_x$  and  $r\text{-Ti}_3\text{C}_2\text{T}_x$ , respectively. Neglecting the small value of contact pad to probe resistance ( $\sim 12\ \Omega$ ) measured in our case, we have used the following relation for total measured resistance:  $R_T = (R_s/W)L + 2R_c$ , where  $R_s$  is the sheet resistance of the films,  $L$  and  $W$  are spacing and width of the metal pads, respectively, and  $R_c$  is the metal pad to MXene film contact resistance. Hence, from slopes of the fitted lines in Fig. 4b and c, we obtained sheet resistance values of  $1415 \pm 125$  and  $288 \pm 27\ \Omega\ \text{sq}^{-1}$  for  $\text{Ti}_3\text{C}_2\text{T}_x$  and  $r\text{-Ti}_3\text{C}_2\text{T}_x$ , respectively. With the measured thicknesses of 1.5 and  $1.2\ \mu\text{m}$  for  $\text{Ti}_3\text{C}_2\text{T}_x$  and  $r\text{-Ti}_3\text{C}_2\text{T}_x$  films (see Fig. S3, ESI†), the corresponding conductivity values are  $471 \pm 49$  and  $2819 \pm 306\ \text{S}\ \text{m}^{-1}$ ,

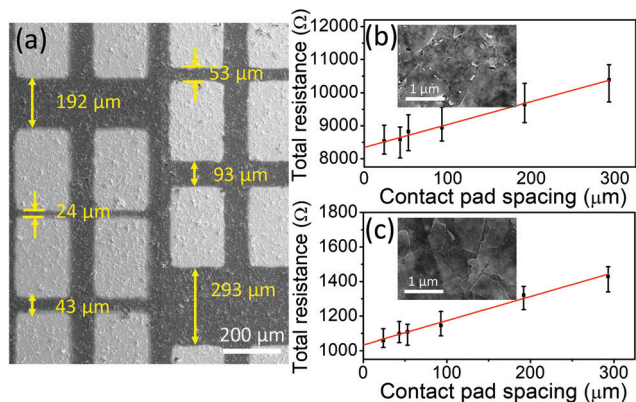


Fig. 4 SEM image of Au/Ti contact pads on r-Ti<sub>3</sub>C<sub>2</sub>T<sub>x</sub> films on SiO<sub>2</sub>/Si (a), plots of total resistance vs. contact pad spacing of (b) Ti<sub>3</sub>C<sub>2</sub>T<sub>x</sub> and (c) r-Ti<sub>3</sub>C<sub>2</sub>T<sub>x</sub> films on SiO<sub>2</sub>/Si. Insets in figures b and c are the high magnification SEM images of the corresponding films.

respectively. The contact resistance of the Ti/Au pad with MXene films obtained from the *y*-intercept values in Fig. 4b and c are  $4.2 \pm 0.4$  and  $0.5 \pm 0.05$  KΩ for Ti<sub>3</sub>C<sub>2</sub>T<sub>x</sub> and r-Ti<sub>3</sub>C<sub>2</sub>T<sub>x</sub> films, respectively, and the corresponding contact resistivities are  $(2.6 \pm 0.3) \times 10^{-4}$  and  $(3.3 \pm 0.4) \times 10^{-5}$  Ω m<sup>2</sup>. These values are high compared to the values for continuous graphene–metal contacts,<sup>42,43</sup> but reasonable considering the nature of the films made by drop casting of the MXene sheets.

Although our conductivity values for Ti<sub>3</sub>C<sub>2</sub>T<sub>x</sub> and r-Ti<sub>3</sub>C<sub>2</sub>T<sub>x</sub> films fall within widely scattered values of 2D titanium carbide MXene films reported previously,<sup>16,24,33,37,44,45</sup> these values are smaller than most of the previously reported values for Ti<sub>3</sub>C<sub>2</sub>T<sub>x</sub>. Since the conductivity of MXene films is synthesis and processing dependent, the relatively small electrical conductivity of our Ti<sub>3</sub>C<sub>2</sub>T<sub>x</sub> can mainly be attributed to the use of HF as an etchant instead of a mixture of HCl and alkali metal fluoride salts such as LiF, as suggested in a published report.<sup>36</sup> Moreover, the choice of intercalant for delamination, flake size and thickness, and film processing method could also alter the conductivity. Most importantly, it is exciting to find that the electrical conductivity of Ti<sub>3</sub>C<sub>2</sub>T<sub>x</sub> is enhanced six-fold upon treatment with L-ascorbic acid, suggesting a great value of the reduction process in MXene processing. Our result suggests that the reduction of Ti<sub>3</sub>C<sub>2</sub>T<sub>x</sub> *via* L-ascorbic treatment significantly enhances the electrical conductivity regardless of the initial conductivity value. An eight-fold reduction in the contact resistivity of r-Ti<sub>3</sub>C<sub>2</sub>T<sub>x</sub> with respect to Ti<sub>3</sub>C<sub>2</sub>T<sub>x</sub> also suggests that r-Ti<sub>3</sub>C<sub>2</sub>T<sub>x</sub> is a more suitable material than Ti<sub>3</sub>C<sub>2</sub>T<sub>x</sub> for fabricating devices that require metal–MXene contacts, such as electronic and optoelectronic devices. The reason for the enhanced conductivity in r-Ti<sub>3</sub>C<sub>2</sub>T<sub>x</sub> can be explained as a consequence of the changes in chemistry of the MXene crystals during HF and L-ascorbic acid treatments. First, the carbon atoms that are replaced by O<sup>2-</sup> ions during the HF etching process<sup>2</sup> are subsequently removed by L-ascorbic acid treatment creating vacancies in the crystal lattice and this provides a localized electron in the vacant site. Next, the XPS result shows that a significant loss of fluorine terminations occurs during the reduction process. These modifications in the

crystal chemistry cause redistribution of the missing hybridized Ti3d–C2p and Ti3d–F2p states to Ti–Ti metallic bond states near the Fermi energy, thereby increasing the DOS at the Fermi level. With this argument, a significantly large electrical conductivity of each r-Ti<sub>3</sub>C<sub>2</sub>T<sub>x</sub> nanosheet is expected compared to an untreated Ti<sub>3</sub>C<sub>2</sub>T<sub>x</sub> sheet.

### 3.3 Oxidation stability

Fig. 5(a–f) show photographs of the aqueous solutions of Ti<sub>3</sub>C<sub>2</sub>T<sub>x</sub> (left) and r-Ti<sub>3</sub>C<sub>2</sub>T<sub>x</sub> (right) collected on different days. We reiterate that the aqueous solutions (15 mg/10 ml) of Ti<sub>3</sub>C<sub>2</sub>T<sub>x</sub> and r-Ti<sub>3</sub>C<sub>2</sub>T<sub>x</sub> were prepared by re-dispersing the dried powders of the corresponding materials in water to study oxidation stability. Both Ti<sub>3</sub>C<sub>2</sub>T<sub>x</sub> and r-Ti<sub>3</sub>C<sub>2</sub>T<sub>x</sub> aqueous solutions look black initially, but upon exposure to water for several days, Ti<sub>3</sub>C<sub>2</sub>T<sub>x</sub> aqueous solution turns whitish faster than r-Ti<sub>3</sub>C<sub>2</sub>T<sub>x</sub> aqueous solution, indicating a faster degradation of Ti<sub>3</sub>C<sub>2</sub>T<sub>x</sub> crystals. The repeated experiment with a lower concentration (5 mg/10 ml) of Ti<sub>3</sub>C<sub>2</sub>T<sub>x</sub> and r-Ti<sub>3</sub>C<sub>2</sub>T<sub>x</sub> in water results in the same observation (see Fig. S4, ESI†). As shown in Fig. 5b, the MXene nanosheets allowed to oxidize for 3 days do not look distinctively different to the eye, but the difference can easily be detected by Raman spectroscopic analysis of the corresponding dried powders (Fig. 5g and h). The features in the Raman spectra for each of Ti<sub>3</sub>C<sub>2</sub>T<sub>x</sub> and r-Ti<sub>3</sub>C<sub>2</sub>T<sub>x</sub> exposed to water for a different

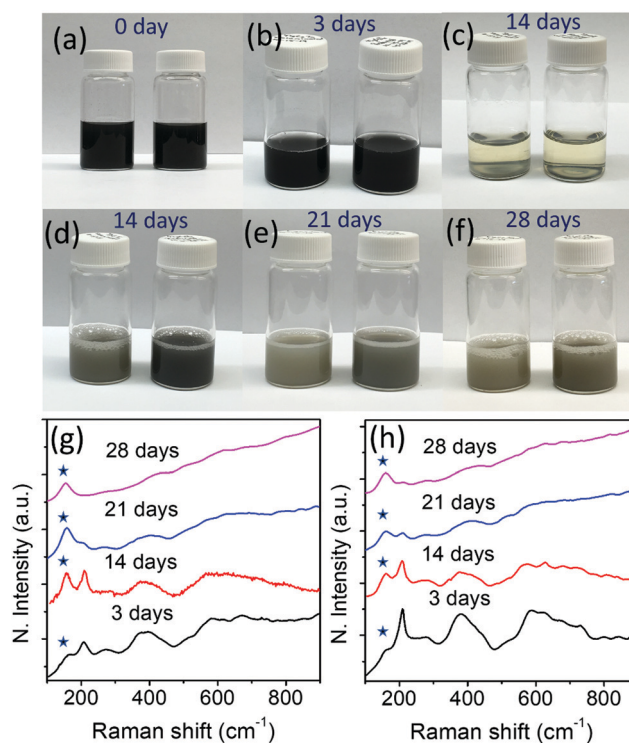


Fig. 5 Photographs of the aqueous solutions of Ti<sub>3</sub>C<sub>2</sub>T<sub>x</sub> (left) and r-Ti<sub>3</sub>C<sub>2</sub>T<sub>x</sub> (right) collected after (a) 0 day, (b) 3 days, (c) 14 days before shaking, (d) 14 days, (e) 21 days, and (f) 28 days. The concentrations of Ti<sub>3</sub>C<sub>2</sub>T<sub>x</sub> and r-Ti<sub>3</sub>C<sub>2</sub>T<sub>x</sub> solutions were 15 mg in 10 ml of water. Normalized Raman spectra collected on dried powder from the aqueous solutions of (g) Ti<sub>3</sub>C<sub>2</sub>T<sub>x</sub>, and (h) r-Ti<sub>3</sub>C<sub>2</sub>T<sub>x</sub> kept for different days.

length of time are different. With the increased number of days, the degraded MXene powders show a gradual increase of the  $E_g$  vibrational band intensity of anatase  $\text{TiO}_2$  occurring at  $\sim 149 \text{ cm}^{-1}$  (indicated with stars) and a decrease of the MXene peak occurring at  $\sim 205 \text{ cm}^{-1}$ , as observed by Zhang *et al.*<sup>31</sup> It is evident from Fig. 5g and h that the ratio of anatase  $\text{TiO}_2$  to MXene band intensities increases faster for  $\text{Ti}_3\text{C}_2\text{T}_x$  than  $r\text{-Ti}_3\text{C}_2\text{T}_x$ , which indicates that  $r\text{-Ti}_3\text{C}_2\text{T}_x$  nanoflakes are more stable in oxygen-rich environments such as water. SEM micrographs (Fig. S5, ESI†) further confirm that nucleation and growth of  $\text{TiO}_2$  nanoparticles take place faster on  $\text{Ti}_3\text{C}_2\text{T}_x$  surfaces than on  $r\text{-Ti}_3\text{C}_2\text{T}_x$  surfaces.

It is evident that after treatment with *L*-ascorbic acid,  $\text{Ti}_3\text{C}_2\text{T}_x$  nanosheets become more stable in the oxygen rich environment. This result is consistent with a recent work<sup>30</sup> that uncovered that  $\text{Ti}_3\text{C}_2\text{T}_x$  nanosheets were protected from severe oxidation up to six months when stored in a sodium ascorbate aqueous solution. The average lateral size of the  $\text{Ti}_3\text{C}_2\text{T}_x$  and  $r\text{-Ti}_3\text{C}_2\text{T}_x$  nanosheets in the SEM images in Fig. S2c, d and S5 presented in the ESI† are  $\sim 1.6$  and  $\sim 1.5 \mu\text{m}$ , respectively. Hence, a faster degradation of  $\text{Ti}_3\text{C}_2\text{T}_x$  nanosheets compared to  $r\text{-Ti}_3\text{C}_2\text{T}_x$  in water is not because of the smaller flake size as reported previously.<sup>31</sup> The enhanced oxidation stability of  $r\text{-Ti}_3\text{C}_2\text{T}_x$  can be explained based on the reduction of the  $\text{Ti}_3\text{C}_2\text{T}_x$  nanosheets caused by *L*-ascorbic acid molecules. As described above,  $\text{O}^{2-}$  ions replace a significantly large number of carbons from the  $\text{Ti}_3\text{C}_2\text{T}_x$  lattice during the Al layer etching process, as shown in Fig. 1b. These oxygen sites in the  $\text{Ti}_3\text{C}_2\text{T}_x$  crystal act as nucleation centers for  $\text{TiO}_2$  nanoparticle growth. Upon exposure of the  $\text{Ti}_3\text{C}_2\text{T}_x$  nanosheets to water,

reactive oxygen species such as hydroxyl radical or oxygen molecules react with the nanosheets breaking the Ti–C bonds and forming Ti–O bonds.<sup>30</sup> This process accelerates the  $\text{TiO}_2$  nanoparticle growth. The carbons released during this process are bonded to each other forming disordered carbon material (see Fig. S6, ESI†). Hence, the MXene nanosheets continue to degrade while  $\text{TiO}_2$  nanoparticles continue to increase in size. This argument is supported by the SEM micrographs (see Fig. S5, ESI†) of the MXene sheets, where  $\text{TiO}_2$  nanoparticles are observed to increase in size with continued exposure to water. The  $\text{TiO}_2$  nanoparticle growth on the MXene surface also confirms that MXene degradation not only starts at the  $\text{Ti}_3\text{C}_2\text{T}_x$  sheet edges as claimed in the literature,<sup>30,31</sup> but it also occurs simultaneously at the basal plane. However, *L*-ascorbic acid treatment on  $\text{Ti}_3\text{C}_2\text{T}_x$  removes the  $\text{O}^{2-}$  ions sitting in the carbon sites, and the possible nucleation sites for  $\text{TiO}_2$  particle growth are minimized. This argument is supported by a much smaller density and size of the  $\text{TiO}_2$  nanoparticles grown on the basal plane of  $r\text{-Ti}_3\text{C}_2\text{T}_x$  compared to  $\text{Ti}_3\text{C}_2\text{T}_x$  (see Fig. S5, ESI†). Such an enhanced oxidation stability makes  $r\text{-Ti}_3\text{C}_2\text{T}_x$  a promising material for use in applications.

### 3.4 SERS activity

Fig. 6a–c show SERS spectra of the probe molecules, crystal violet (CV) at  $2 \times 10^{-6} \text{ M}$ , methylene blue (MB) at  $1 \times 10^{-6} \text{ M}$ , and rhodamine 6G (R6G) at  $1 \times 10^{-7} \text{ M}$ , respectively, collected on  $\text{Ti}_3\text{C}_2\text{T}_x/\text{SiO}_2/\text{Si}$  (black) and  $r\text{-Ti}_3\text{C}_2\text{T}_x/\text{SiO}_2/\text{Si}$  (red) substrates. It is apparent that the  $r\text{-Ti}_3\text{C}_2\text{T}_x/\text{SiO}_2/\text{Si}$  substrate shows about an order of magnitude higher Raman signal intensity compared to  $\text{Ti}_3\text{C}_2\text{T}_x/\text{SiO}_2/\text{Si}$  for all three probe molecules.

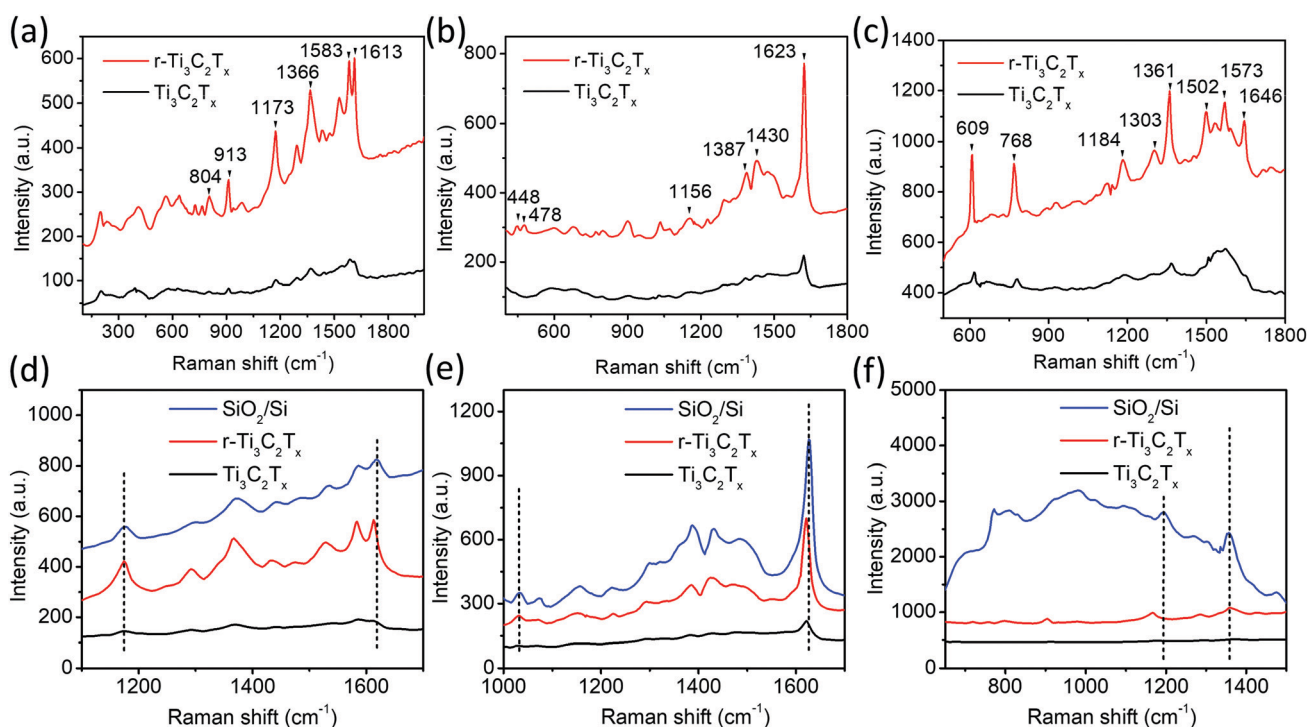


Fig. 6 SERS spectra of (a and d) CV, (b and e) MB, and (c and f) R6G collected on  $\text{Ti}_3\text{C}_2\text{T}_x/\text{SiO}_2/\text{Si}$  (black) and  $r\text{-Ti}_3\text{C}_2\text{T}_x/\text{SiO}_2/\text{Si}$  (red), and bare  $\text{SiO}_2/\text{Si}$  (blue) substrates. Concentration of dyes on  $\text{SiO}_2/\text{Si}$  substrate is 1 M in water.



Table 1 Calculated analytical Raman enhancement factors for CV, MB, and R6G

Probe molecules	SERS substrates	Raman shift (cm <sup>-1</sup> )	Peak assignment	Dye concentration (M)	EF
CV	Ti <sub>3</sub> C <sub>2</sub> T <sub>x</sub> /SiO <sub>2</sub> /Si	1613	In-plane stretching of C–C ring <sup>46</sup>	2.0 × 10 <sup>-6</sup>	2.1 × 10 <sup>5</sup>
	r-Ti <sub>3</sub> C <sub>2</sub> T <sub>x</sub> /SiO <sub>2</sub> /Si				1.6 × 10 <sup>6</sup>
MB	Ti <sub>3</sub> C <sub>2</sub> T <sub>x</sub> /SiO <sub>2</sub> /Si	1623	In-plane stretching of C–C ring <sup>47</sup>	1.0 × 10 <sup>-6</sup>	1.0 × 10 <sup>5</sup>
	r-Ti <sub>3</sub> C <sub>2</sub> T <sub>x</sub> /SiO <sub>2</sub> /Si				7.8 × 10 <sup>5</sup>
R6G	Ti <sub>3</sub> C <sub>2</sub> T <sub>x</sub> /SiO <sub>2</sub> /Si	1361	Carboxylate stretches <sup>48</sup>	1.0 × 10 <sup>-7</sup>	1.3 × 10 <sup>6</sup>
	r-Ti <sub>3</sub> C <sub>2</sub> T <sub>x</sub> /SiO <sub>2</sub> /Si				1.0 × 10 <sup>7</sup>

Raman enhancement on SERS substrates prepared with Ti<sub>3</sub>C<sub>2</sub>T<sub>x</sub> and r-Ti<sub>3</sub>C<sub>2</sub>T<sub>x</sub> on PVDF filter membrane (see photographs Fig. S7, ESI†) showed similar results.

The SERS EF was calculated using the following equation:  $EF = (I_{SERS}/C_{SERS})/(I_{ref}/C_{ref})$ , where  $I_{SERS}$  is the Raman intensity of a selected vibrational mode of a dye with a concentration of  $C_{SERS}$ , and  $I_{ref}$  is the intensity of the same vibrational mode of the dye on a SERS inactive substrate (SiO<sub>2</sub>/Si) with a concentration of  $C_{ref}$ . The calculated SERS EFs for different dyes are presented in Table 1.

It is evident that the SERS EF is an order of magnitude higher on r-Ti<sub>3</sub>C<sub>2</sub>T<sub>x</sub>/SiO<sub>2</sub>/Si than on Ti<sub>3</sub>C<sub>2</sub>T<sub>x</sub>/SiO<sub>2</sub>/Si for all three dyes used. The calculated SERS EFs for Ti<sub>3</sub>C<sub>2</sub>T<sub>x</sub>/SiO<sub>2</sub>/Si are similar to that of the SERS substrates fabricated with Ti<sub>3</sub>C<sub>2</sub>T<sub>x</sub> on glass and silicon in the literature<sup>20</sup> and are much larger than those of Ti<sub>2</sub>NT<sub>x</sub>-based SERS substrates fabricated on glass and silicon reported by Soundiraraju *et al.*<sup>4</sup>

As shown in Fig. 6d–f, some of the vibrational peak positions in the SERS spectra of CV, MB, and R6G are red-shifted with respect to their original positions, *i.e.*, Raman peak positions measured on the non-SERS substrate, SiO<sub>2</sub>/Si. For example, the in-plane stretching mode of the C–C ring of CV and MB appears at 1619 and 1629 cm<sup>-1</sup> on SiO<sub>2</sub>/Si, respectively, which shift to 1613 and 1623 cm<sup>-1</sup> on MXene substrates. For R6G, the peak associated with the in-plane stretching mode of C–C ring appears at 1196 cm<sup>-1</sup> on bare SiO<sub>2</sub>/Si, which is shifted to 1187 cm<sup>-1</sup> on MXene substrates. We also noticed that there was no shift in some peaks, such as those appearing at 1173 cm<sup>-1</sup> and 1032 cm<sup>-1</sup> corresponding to the in-plane bending mode of C–H in CV<sup>46</sup> and MB,<sup>47</sup> respectively, and 1361 cm<sup>-1</sup> corresponding to the carboxylate stretch mode<sup>48</sup> in R6G. The shift in the peak positions of dye molecules on Ti<sub>3</sub>C<sub>2</sub>T<sub>x</sub> and r-Ti<sub>3</sub>C<sub>2</sub>T<sub>x</sub> SERS substrates is attributed to charge transfer interaction<sup>49,50</sup> of the MXenes with the probe molecules. To understand our results, it is reasonable to expect the transfer of electrons from electron rich MXenes to C–C rings of the dye molecules, which slightly weakens C–C bonds of the rings, causing a red-shift of the associated vibrational peaks. However, no charge transfer from MXenes to the C–H bond of CV and MB, and to the carboxylate group of R6G takes place. Hence, a peak shift associated with these bonds was not observed. Band shift due to charge transfer interaction is common in several other spectroscopies, such as XPS,<sup>51</sup> nuclear magnetic resonance spectroscopy,<sup>52</sup> and infrared absorption spectroscopy (IR).<sup>52,53</sup> In Raman spectroscopy, the degree of charge transfer is reflected by the magnitude of wavenumber shift<sup>53,54</sup> and has a positive correlation with Raman signal enhancement.<sup>55</sup> Hence, based on the magnitude of the band shift,

the degree of the charge transfer is found to be slightly greater in R6G than in CV and MB. This is supported by the higher Raman EF of R6G compared to those of CV and MB. Moreover, the laser excitation wavelength, 532 nm, is much closer to the light absorption peak position of R6G (527 nm) (see Fig. S8 for UV visible spectra, ESI†) than the absorption peak positions of CV (591 nm) and MB (663 nm). Hence, the matching of the excitation beam energy with a molecular transition is another factor that accounts for the higher EF of R6G than those of CV and MB.

Now, we discuss briefly why the r-Ti<sub>3</sub>C<sub>2</sub>T<sub>x</sub>/SiO<sub>2</sub>/Si SERS substrate enhances the Raman signal of dye molecules more than the Ti<sub>3</sub>C<sub>2</sub>T<sub>x</sub>/SiO<sub>2</sub>/Si substrate. As mentioned above, L-ascorbic acid treatment removes more than 50% of the F terminations on Ti<sub>3</sub>C<sub>2</sub>T<sub>x</sub>, exposing a much larger number of surface-Ti atoms to the adsorbing dye molecules. This allows a larger population of adsorbing dye molecules to interact and form charge transfer complexes with r-Ti<sub>3</sub>C<sub>2</sub>T<sub>x</sub>. Consequently, a higher EF factor is achieved. Additionally, as described above, the increased electronic DOS at the Fermi level in r-Ti<sub>3</sub>C<sub>2</sub>T<sub>x</sub> facilitates electronic charge transfer to dye molecules, causing an enhanced Raman EF. Despite the increased metallic property or DOS at the Fermi level in r-Ti<sub>3</sub>C<sub>2</sub>T<sub>x</sub>, no plasmonic absorption was observed in the UV visible spectrum (see Fig. S9, ESI†). Hence, the observed SERS enhancement of the dye molecules cannot be attributed directly to the electromagnetic contribution.

## 4. Conclusions

We have developed a facile and green protocol for the room temperature synthesis of reduced Ti<sub>3</sub>C<sub>2</sub>T<sub>x</sub> MXene nanosheets *via* a simple treatment with L-ascorbic acid. The results show that r-Ti<sub>3</sub>C<sub>2</sub>T<sub>x</sub> has a 6-fold higher electrical conductivity and has a better oxidation stability than Ti<sub>3</sub>C<sub>2</sub>T<sub>x</sub>, making r-Ti<sub>3</sub>C<sub>2</sub>T<sub>x</sub> a more promising material for most applications. Furthermore, r-Ti<sub>3</sub>C<sub>2</sub>T<sub>x</sub> offers a much smaller contact resistance with Ti/Au contact pads, which encourages the use of r-Ti<sub>3</sub>C<sub>2</sub>T<sub>x</sub> in fabricating devices that require metal-MXene contacts, such as electronic and optoelectronic devices.

The study demonstrates that r-Ti<sub>3</sub>C<sub>2</sub>T<sub>x</sub> enhances the Raman signal of dye molecules by an order of magnitude compared to Ti<sub>3</sub>C<sub>2</sub>T<sub>x</sub>. The SERS enhancement factor obtained for R6G on r-Ti<sub>3</sub>C<sub>2</sub>T<sub>x</sub> is as high as 10<sup>7</sup> using the laser excitation wavelength of 532 nm, indicating a potential use of r-Ti<sub>3</sub>C<sub>2</sub>T<sub>x</sub> for making practical SERS substrates. The outstanding SERS activity of r-Ti<sub>3</sub>C<sub>2</sub>T<sub>x</sub> has been attributed to a larger number of Ti atoms

exposed due to the loss of F terminations allowing a larger population of dye molecules to interact with  $r\text{-Ti}_3\text{C}_2\text{T}_x$ . The higher SERS activity of  $r\text{-Ti}_3\text{C}_2\text{T}_x$  is further re-enforced by the increased electronic DOS at the Fermi level. The findings of this study suggest that reduced MXene could be a superior choice over MXene prepared by regular methods, especially for applications that employ high electronic conductivity, such as electrode materials for batteries and supercapacitors, photodetectors, and SERS-based sensors.

## Abbreviations

2D	Two-dimensional
TMAOH	Tetramethylammonium hydroxide
Li-EDA	Li-ethylenediamine
$r\text{-Ti}_3\text{C}_2\text{T}_x$	Reduced $\text{Ti}_3\text{C}_2\text{T}_x$ MXene
CV	Crystal violet
MB	Methylene blue
R6G	Rhodamine 6G
SERS	Surface-enhanced Raman scattering
AFM	Atomic force microscopy
SEM	Scanning electron microscopy
TEM	Transmission electron microscopy
SAED	Selected area electron diffraction
XPS	X-ray photoelectron spectroscopy
XRD	X-ray diffractometry

## Conflicts of interest

The authors declare no competing financial interest.

## Acknowledgements

The authors are grateful for the financial support of this project by the U.S. National Science Foundation (Awards # 1831133 and #1523617). Q. L. and S. K. would like to thank NSF Award #1905833 and DOE FG02-08ER46531. This work was performed in part at the Analytical Instrumentation Facility (AIF) and Nanofabrication facility (NNF) at North Carolina State University, which is supported by the State of North Carolina and the National Science Foundation (award number ECCS-1542015). The AIF and NNF are members of the North Carolina Research Triangle Nanotechnology Network (RTNN), a site in the National Nanotechnology Coordinated Infrastructure (NNCI). The authors thank Dr Spyridon Pavlidis and Mr Rohan Sengupta for assisting in electrical measurements.

## References

- M. Naguib, M. Kurtoglu, V. Presser, J. Lu, J. Niu, M. Heon, L. Hultman, Y. Gogotsi and M. W. Barsoum, *Adv. Mater.*, 2011, **23**, 4248.
- Y. Yoon, T. A. Le, A. P. Tiwari, I. Kim, M. W. Barsoum and H. Lee, *Nanoscale*, 2018, **10**, 22429.
- K. Chaudhuri, M. Alhabeab, Z. Wang, V. M. Shalae, Y. Gogotsi and A. Boltasseva, *ACS Photonics*, 2018, **5**, 1115.
- B. Soundiraraju and B. K. George, *ACS Nano*, 2017, **11**, 8892.
- M. H. Tran, T. Schäfer, A. Shahraei, M. Dürrschnabel, L. Molina-Luna, U. I. Kramm and C. S. Birkel, *ACS Appl. Energy Mater.*, 2018, **1**, 3908.
- J. L. Hart, K. Hantanasirisakul, A. C. Lang, B. Anasori, D. Pinto, Y. Pivak, J. T. van Omme, S. J. May, Y. Gogotsi and M. L. Taheri, *Nat. Commun.*, 2019, **10**, 522.
- L. Verger, V. Natu, M. Carey and M. W. Barsoum, *Trends Chem.*, 2019, **1**, 656.
- M. Naguib, O. Mashtalir, J. Carle, V. Presser, J. Lu, L. Hultman, Y. Gogotsi and M. W. Barsoum, *ACS Nano*, 2012, **6**, 1322.
- M. Khazaei, M. Arai, T. Sasaki, C.-Y. Chung, N. S. Venkataramanan, M. Estili, Y. Sakka and Y. Kawazoe, *Adv. Funct. Mater.*, 2013, **23**, 2185.
- M. R. Lukatskaya, O. Mashtalir, C. E. Ren, Y. Dall'Agnese, P. Rozier, P. L. Taberna, M. Naguib, P. Simon, M. W. Barsoum and Y. Gogotsi, *Science*, 2013, **341**, 1502.
- M. Ghidui, M. R. Lukatskaya, M.-Q. Zhao, Y. Gogotsi and M. W. Barsoum, *Nature*, 2014, **516**, 78.
- Q. Pan, C. Duan, H. Liu, M. Li, Z. Zhao, D. Zhao, Y. Duan, Y. Chen and Y. Wang, *ACS Appl. Energy Mater.*, 2019, **2**, 6834.
- G. Gao, A. P. O'Mullane and A. Du, *ACS Catal.*, 2017, **7**, 494.
- Z. W. Seh, K. D. Fredrickson, B. Anasori, J. Kibsgaard, A. L. Strickler, M. R. Lukatskaya, Y. Gogotsi, T. F. Jaramillo and A. Vojvodic, *ACS Energy Lett.*, 2016, **1**, 589.
- C. E. Ren, K. B. Hatzell, M. Alhabeab, Z. Ling, K. A. Mahmoud and Y. Gogotsi, *J. Phys. Chem. Lett.*, 2015, **6**, 4026.
- C. (John) Zhang, B. Anasori, A. Seral-Ascaso, S.-H. Park, N. McEvoy, A. Shmeliov, G. S. Duesberg, J. N. Coleman, Y. Gogotsi and V. Nicolosi, *Adv. Mater.*, 2017, **29**, 1702678.
- G. Ying, A. D. Dillon, A. T. Fafarman and M. W. Barsoum, *Mater. Res. Lett.*, 2017, **5**, 391.
- J. Liu, H.-B. Zhang, R. Sun, Y. Liu, Z. Liu, A. Zhou and Z.-Z. Yu, *Adv. Mater.*, 2017, **29**, 1702367.
- D. B. Velusamy, J. K. El-Demellawi, A. M. El-Zohry, A. Giugni, S. Lopatin, M. N. Hedhili, A. E. Mansour, E. D. Fabrizio, O. F. Mohammed and H. N. Alshareef, *Adv. Mater.*, 2019, **31**, 1807658.
- A. Sarycheva, T. Makaryan, K. Maleski, E. Satheeshkumar, A. Melikyan, H. Minassian, M. Yoshimura and Y. Gogotsi, *J. Phys. Chem. C*, 2017, **121**, 19983.
- E. Satheeshkumar, T. Makaryan, A. Melikyan, H. Minassian, Y. Gogotsi and M. Yoshimura, *Sci. Rep.*, 2016, **6**, 32049.
- K. Hantanasirisakul, M. Alhabeab, A. Lipatov, K. Maleski, B. Anasori, P. Salles, C. Ieosakulrat, P. Pakawatpanurut, A. Sinitskii, S. J. May and Y. Gogotsi, *Chem. Mater.*, 2019, **31**, 2941.
- R. Li, L. Zhang, L. Shi and P. Wang, *ACS Nano*, 2017, **11**, 3752.
- Z. Ling, C. E. Ren, M.-Q. Zhao, J. Yang, J. M. Giammarco, J. Qiu, M. W. Barsoum and Y. Gogotsi, *Proc. Natl. Acad. Sci. U. S. A.*, 2014, **111**, 16676.
- Y. Xie and P. R. C. Kent, *Phys. Rev. B: Condens. Matter Mater. Phys.*, 2013, **87**, 235441.
- M. Savchak, N. Borodinov, R. Burtovyy, M. Anayee, K. Hu, R. Ma, A. Grant, H. Li, D. B. Cutshall, Y. Wen, G. Koley,

- W. R. Harrell, G. Chumanov, V. Tsukruk and I. Luzinov, *ACS Appl. Mater. Interfaces*, 2018, **10**, 3975.
- 27 Y. Chen, K. Fu, S. Zhu, W. Luo, Y. Wang, Y. Li, E. Hitz, Y. Yao, J. Dai, J. Wan, V. A. Danner, T. Li and L. Hu, *Nano Lett.*, 2016, **16**, 3616.
- 28 X. Xie, Y. Zhu, F. Li, X. Zhou and T. Xue, *Sci. China: Technol. Sci.*, 2019, **62**, 1202.
- 29 K. Kneipp, Y. Wang, H. Kneipp, L. T. Perelman, I. Itzkan, R. R. Dasari and M. S. Feld, *Phys. Rev. Lett.*, 1997, **78**, 1667.
- 30 X. Zhao, A. Vashisth, E. Prehn, W. Sun, S. A. Shah, T. Habib, Y. Chen, Z. Tan, J. L. Lutkenhaus, M. Radovic and M. J. Green, *Matter*, 2019, **1**, 513.
- 31 C. J. Zhang, S. Pinilla, N. McEvoy, C. P. Cullen, B. Anasori, E. Long, S.-H. Park, A. Seral-Ascaso, A. Shmeliov, D. Krishnan, C. Morant, X. Liu, G. S. Duesberg, Y. Gogotsi and V. Nicolosi, *Chem. Mater.*, 2017, **29**, 4848.
- 32 T. Habib, X. Zhao, S. A. Shah, Y. Chen, W. Sun, H. An, J. L. Lutkenhaus, M. Radovic and M. J. Green, *npj 2D Mater. Appl.*, 2019, **3**, 8.
- 33 A. Lipatov, M. Alhabeb, M. R. Lukatskaya, A. Boson, Y. Gogotsi and A. Sinitskii, *Adv. Electron. Mater.*, 2016, **2**, 1600255.
- 34 H. Ghassemi, W. Harlow, O. Mashtalir, M. Beidaghi, M. R. Lukatskaya, Y. Gogotsi and M. L. Taheri, *J. Mater. Chem. A*, 2014, **2**, 14339.
- 35 V. Natu, J. L. Hart, M. Sokol, H. Chiang, M. L. Taheri and M. W. Barsoum, *Angew. Chem., Int. Ed.*, 2019, **58**, 12655.
- 36 M. Alhabeb, K. Maleski, B. Anasori, P. Lelyukh, L. Clark, S. Sin and Y. Gogotsi, *Chem. Mater.*, 2017, **29**, 7633.
- 37 A. Pazniak, P. Bazhin, N. Shplis, E. Kolesnikov, I. Shchetinin, A. Komissarov, J. Polcak, A. Stolin and D. Kuznetsov, *Mater. Des.*, 2019, **183**, 108143.
- 38 J. Halim, K. M. Cook, M. Naguib, P. Eklund, Y. Gogotsi, Y. Rosen and J. Barsoum, *Appl. Surf. Sci.*, 2016, **30**, 406–417.
- 39 Y. Zhang, Z. Xing, X. Liu, Z. Li, X. Wu, J. Jiang, M. Li, Q. Zhu and W. Zhou, *ACS Appl. Mater. Interfaces*, 2016, **8**, 26851.
- 40 V. Presser, M. Naguib, L. Chaput, A. Togo, G. Hug and M. W. Barsoum, *J. Raman Spectrosc.*, 2012, **43**, 168.
- 41 O. Frank, M. Zukalova, B. Laskova, J. Kürti, J. Koltai and L. Kavan, *Phys. Chem. Chem. Phys.*, 2012, **14**, 14567.
- 42 S. Min Song, T. Yong Kim, O. Jae Sul, W. Cheol Shin and B. Jin Cho, *Appl. Phys. Lett.*, 2014, **104**, 183506.
- 43 V. Passi, A. Gahoi, E. G. Marin, T. Cusati, A. Fortunelli, G. Iannaccone, G. Fiori and M. C. Lemme, *Adv. Mater. Interfaces*, 2019, **6**, 1801285.
- 44 J. Halim, M. R. Lukatskaya, K. M. Cook, J. Lu, C. R. Smith, L.-Å. Näslund, S. J. May, L. Hultman, Y. Gogotsi, P. Eklund and M. W. Barsoum, *Chem. Mater.*, 2014, **26**, 2374.
- 45 H. Kitadai, X. Wang, N. Mao, S. Huang and X. Ling, *J. Phys. Chem. Lett.*, 2019, **10**, 3043.
- 46 L. Pei, Y. Huang, C. Li, Y. Zhang, B. A. Rasco and K. Lai, *J. Nanomater.*, 2014, 730915.
- 47 K.-D. Shim and E.-S. Jang, *Bull. Korean Chem. Soc.*, 2018, **39**, 936.
- 48 M. Liu, M. Liu, Y. Shi, Y. Shi, G. Zhang, G. Zhang, Y. Zhang, M. Wu, J. Ren and B. Man, *Appl. Spectrosc.*, 2018, **72**, 1613.
- 49 Y. Wang, W. Ji, H. Sui, Y. Kitahama, W. Ruan, Y. Ozaki and B. Zhao, *J. Phys. Chem. C*, 2014, **118**, 10191.
- 50 S. Liu, Y. Li, X. Zhao, X. Liu and M. Chen, *Spectrochim. Acta, Part A*, 2011, **82**, 205.
- 51 C. Lenser, Q. Lu, E. Crumlin, H. Bluhm and B. Yildiz, *J. Phys. Chem. C*, 2018, **122**, 4841.
- 52 M. S. Refat, H. A. Saad, A. M. A. Adam, M. A. Al-Omar and A. M. Naglah, *Acta Pharm.*, 2016, **66**, 533.
- 53 T. B. Limbu, F. Mendoza, D. Barrionuevo, J. Carpena, B. Maruyama, R. S. Katiyar, B. R. Weiner and G. Morell, *AIP Adv.*, 2016, **6**, 035319.
- 54 A. C. Crowther, A. Ghassaei, N. Jung and L. E. Brus, *ACS Nano*, 2012, **6**, 1865.
- 55 H. Kitadai, X. Wang, N. Mao, S. Huang and X. Ling, *J. Phys. Chem. Lett.*, 2019, **10**, 3043.